ELSEVIER

Contents lists available at ScienceDirect

Journal of Computational Physics

www.elsevier.com/locate/jcp



A cost-effective semi-implicit method for the time integration of fully compressible reacting flows with stiff chemistry



Guillaume Beardsell*, Guillaume Blanguart

Department of Mechanical Engineering, California Institute of Technology, Pasadena, USA

ARTICLE INFO

Article history: Received 17 July 2019 Received in revised form 25 March 2020 Accepted 13 April 2020 Available online 21 April 2020

Keywords: Time integration Detailed chemistry Compressible reacting flows Semi-implicit correction

ABSTRACT

We present a simple method to remove the stiffness associated with the chemical source terms in the fully compressible Navier-Stokes equations when the classical fourth order Runge-Kutta scheme is used.

© 2020 Elsevier Inc. All rights reserved.

1. Introduction

Reacting flow simulations with detailed chemistry can be computationally challenging because of the extremely short time scales associated with fast chemical reactions [1,2]. When using explicit time integration schemes, this can severely limit the maximum stable timestep, which can in turn dramatically increase the computational cost. The focus of this paper is on alleviating the stiffness associated with the chemical source term $\dot{\omega}_{\rm S}$ in the species transport equations (see Eq. (4)). Consider a laminar n-heptane/air flame at standard thermodynamic conditions and an equivalence ratio $\phi=0.9$, solved with a standard detailed chemical model (see Mechanism #1 in Sec. 2). The maximum stable timesteps associated with the different terms in the Navier-Stokes and species transport equations are: $\Delta t=5\cdot 10^{-10}$ s for chemistry, $\Delta t=2\cdot 10^{-8}$ s for acoustics, $\Delta t=2\cdot 10^{-7}$ s for diffusive and viscous effects, and $\Delta t=10^{-6}$ s for convection. The maximum stable timestep associated with chemistry is estimated by computing the eigenvalues of the chemical Jacobian at the location of maximum heat release. For convection, diffusive/viscous effects, and acoustics, the maximum stable timesteps are obtained by assuming a minimum of 20 points per flame thickness, and a maximum CFL number of 1. These numbers do not vary much among hydrocarbon fuels, except for the maximum stable timestep associated with chemistry, which depends on the chemical mechanism employed. In many cases, chemistry is the most limiting phenomenon in terms of the maximum stable timestep.

For the case considered here, one could use a timestep more than one order of magnitude larger if the chemistry timestep restriction was lifted. To remove this restriction, one can modify the chemical mechanism beforehand. Popular approaches include Computational Singular Perturbation (CSP) [3], Intrinsic Low Dimensional Manifold (ILDM) [4], the Quasi-Steady-State (QSS) approximation, and the Partial Equilibrium (PE) approximation [1]. In all these techniques, the chemical system is altered to alleviate its stiffness, which requires one to make assumptions that might affect the quality of the

^{*} Corresponding author.

E-mail address: gbeardse@caltech.edu (G. Beardsell).

solution. Instead of modifying the chemical mechanism, one can choose time integrators for chemistry that are well suited for stiff systems. Common techniques include operator splitting, in which the transport and reaction terms are treated separately, e.g., by using a stiff ordinary differential equation integrator for chemistry, such as CVODE [5]. Unfortunately, this decouples chemistry and transport, which can lead to so-called splitting errors [6]. Following what Savard et al. [2] have done under the low Mach number approximation, one can perform an implicit correction on the chemistry source term by computing an approximation of the chemical Jacobian. However, for compressible reacting flows, explicit time integration schemes are often preferred [7] for their high order of accuracy at an affordable computational cost. While a high order of temporal accuracy is preferred to resolve the transport of acoustic waves [8], it is usually not needed for the transport of species. That is why, second order time integrators are commonly used for reacting flows when the low Mach number approximation is employed [2], i.e., when acoustics are absent.

In summary, for fully compressible flows, one would ideally like to use an implicit scheme for the species transport equations, and a high order, explicit scheme for the continuity, momentum, and energy equations. This is the goal of this work. We extend the method proposed by Savard et al. [2] for fully compressible flows, by combining a second order semi-implicit midpoint scheme for the transport of species with the classical fourth-order accurate Runge-Kutta (RK4) scheme for the other flow variables. Notably, this approach 1) does not require the chemical mechanism to be altered, and 2) integrates the governing equations in a coupled fashion. The RK4 scheme is chosen since it allows for a straightforward coupling with the midpoint scheme.

2. Methodology

2.1. Governing equations

We consider the fully compressible Navier-Stokes equations for reacting flows. The continuity, momentum, energy, and species transport equations are given by

$$\frac{\partial \rho}{\partial t} + \nabla \cdot (\rho \mathbf{u}) = 0, \tag{1}$$

$$\frac{\partial \rho \mathbf{u}}{\partial t} + \nabla \cdot (\rho \mathbf{u} \otimes \mathbf{u}) = -\nabla p + \nabla \cdot \boldsymbol{\tau} \,, \tag{2}$$

$$\frac{\partial \rho e_t}{\partial t} + \nabla \cdot (\boldsymbol{u} \left(\rho e_t + p\right)) = -\nabla \cdot \boldsymbol{q} + \nabla \cdot (\boldsymbol{\tau} \cdot \boldsymbol{u}) , \qquad (3)$$

$$\frac{\partial \rho Y_s}{\partial t} + \nabla \cdot (\rho \mathbf{u} Y_s) = -\nabla \cdot \mathbf{j}_s + \rho \dot{\omega}_s, \qquad s = 1, ..., n_s,$$

$$\tag{4}$$

where $\boldsymbol{\tau} = \mu(\nabla \boldsymbol{u} + (\nabla \boldsymbol{u})^T - 2/3(\nabla \cdot \boldsymbol{u})\boldsymbol{I})$ is the viscous stress tensor, e_t is the total energy, $\boldsymbol{q} = -\lambda \nabla T + \sum_s h_s \boldsymbol{j}_s$ is the heat diffusion flux, n_s is the number of species transported, and Y_s , \boldsymbol{j}_s , $\dot{\omega}_s$ are the mass fraction, diffusion flux, and chemical source term of species s. Equations (1) to (4) are solved using a compressible formulation [9] of the finite-difference solver NGA [10]. The system of governing equations is closed with the ideal gas law $p = \rho RT/W$, where R is the universal gas constant, and W is the molecular weight of the mixture. The species viscosities μ_i are obtained from standard gas kinetic theory, and the mixture-averaged viscosity μ is calculated using a modified form of Wilke's formula [11]. The species thermal diffusivities are evaluated with a modified version of Eucken's formula. The focus of this work being placed on the time integration, the Lewis number of all species is set to unity. Temperature T is not known explicitly, and an implicit equation is solved using Newton's method

$$T_{m+1} = T_m + \left(\frac{\rho R T_m}{W} - \left(\rho \sum_{s=1}^{n_s} h_s(T_m) Y_s - \rho e_t + \frac{1}{2} \rho u u\right)\right) / \left(\rho \sum_{s=1}^{n_s} c_{v,s}(T_m) Y_s\right), \tag{5}$$

where h_s and $c_{v,s}$ are the species enthalpies and heat capacities at constant volume, respectively, and m is the iteration number. Equation (5) is solved until the desired convergence is achieved (close to machine precision), and T_1 is taken to be the converged temperature at the previous sub-iteration/timestep. Pressure p is then obtained via the ideal gas law.

2.2. Time integration

In the next paragraphs, we first briefly summarize the semi-implicit midpoint method proposed by Savard et al. [2]. We then describe how it can be used to transport the species mass fractions, while the RK4 scheme is used for the other transported flow variables, i.e., mass, momentum, and energy.

2.2.1. Iterative explicit midpoint method

The iterative explicit midpoint scheme applied to Eq. (4) yields

$$(\rho \mathbf{Y})_{k+1}^{n+1} = (\rho \mathbf{Y})^n + \Delta t \left[\mathbf{C}_k^* + \mathbf{D}_k^* + \mathbf{\Omega}_k^* \right], \qquad s = 1, ..., n_s$$

$$(6)$$

where C, D, and Ω are the discretized convection, diffusion, and chemical source terms, respectively. The superscripts refer to the timestep at which the quantities are evaluated, n being the current timestep, while starred quantities are evaluated at the half timestep, e.g., $\Omega_k^* = \Omega(Y_k^*)$, with $Y_k^* = (Y_k^{n+1} + Y^n)/2$. The subscripts refer to the sub-iteration number, k being the current sub-iteration.

2.2.2. Semi-implicit correction

Chemistry being the most limiting phenomenon regarding the maximum stable timestep, we seek to perform an implicit correction on Ω , i.e., we want to compute Ω_{k+1}^* instead of Ω_k^* in Eq. (6). In practice, this can be done by evaluating

$$(\rho \mathbf{Y})_{k+1}^{n+1} = (\rho \mathbf{Y})^n + \Delta t \left[\mathbf{C}_k^* + \mathbf{D}_k^* + \mathbf{\Omega}_k^* + \frac{1}{2} \left(\frac{\partial \mathbf{\Omega}}{\partial (\rho \mathbf{Y})} \right)_k^* \left((\rho \mathbf{Y})_{k+1}^{n+1} - (\rho \mathbf{Y})_k^{n+1} \right) \right], \tag{7}$$

where $(\partial \Omega/\partial (\rho Y))_k^*$ is the chemical Jacobian. We can rewrite Eq. (7) as

$$(\rho \mathbf{Y})_{k+1}^{n+1} = (\rho \mathbf{Y})_{k}^{n+1} - \left(\mathbf{I} - \frac{\Delta t}{2} \left(\frac{\partial \mathbf{\Omega}}{\partial \rho \mathbf{Y}}\right)_{k}^{*}\right)^{-1} \cdot \boldsymbol{\theta}_{k} = (\rho \mathbf{Y})_{k}^{n+1} - \left(\mathbf{J}_{k}\right)^{-1} \cdot \boldsymbol{\theta}_{k}, \tag{8}$$

where J_k acts as a preconditioner on the residual of Eq. (6) at the current sub-iteration

$$\boldsymbol{\theta}_k \equiv (\rho \boldsymbol{Y})_k^{n+1} - (\rho \boldsymbol{Y})^n - \Delta t \left[\boldsymbol{C}_k^* + \boldsymbol{D}_k^* + \boldsymbol{\Omega}_k^* \right]. \tag{9}$$

As discussed in more detail by Savard et al. [2], the choice of J_k is somewhat arbitrary and affects the convergence properties only, e.g., setting $J_k = I$ yields the iterative explicit method. One can compute J_k according to Eq. (8) [12], which yields a fully implicit formulation for the chemical source term. However, this can be computationally expensive, since the chemical Jacobian is a full matrix, and J_k needs to be computed and inverted at each sub-iteration. It is simpler and faster to use the idea proposed by Savard et al. [2], which is to approximate the diagonal of the chemical Jacobian, i.e., set

$$\boldsymbol{J}_{k} = \boldsymbol{I} + \frac{\Delta t}{2} \left(\frac{\dot{\omega}_{s}^{-}}{Y_{s}} \right)_{k}^{*}, \tag{10}$$

where $\dot{\omega}_s^-$ is the consumption rate of species s. This is a very good approximation of the diagonal of $[\partial \Omega/\partial (\rho Y)]_k^*$ since the production rate of a species $\dot{\omega}_s^+$ is usually not a function of its own mass fraction, and $\dot{\omega}_s^-$ is usually linear in the species mass fraction, i.e.,

$$\frac{\partial \rho \dot{\omega}_{s}}{\partial (\rho Y)_{s}} = \frac{\partial \rho \dot{\omega}_{s}^{+}}{\partial (\rho Y)_{s}} - \frac{\partial \rho \dot{\omega}_{s}^{-}}{\partial (\rho Y)_{s}} \approx 0 - \frac{\dot{\omega}_{s}^{-}}{Y_{s}}.$$
(11)

Note that since one has to compute $\dot{\omega}_s^-$ to get Ω_s , this approach only amounts to one extra division applied to the residuals of the species transport equations. This approximation is expected to perform extremely well since the maximum timestep due to the acoustics is small, see Secs. 5.1 to 5.3 in [2].

2.2.3. Embedding within the RK4 scheme

The RK4 scheme requires the evaluation of the time derivative at the half timestep (2nd and 3rd stages) and at the full timestep (4th stage). The iterative midpoint method yields both, hence we can embed the midpoint method within the RK4 scheme in a straightforward manner. Note that we still solve for the flow variables $\mathbf{Q} = [\rho, \rho \mathbf{u}, \rho e_t]$ with the RK4 scheme. The proposed method is detailed below:

Step	Function evaluation	Flow (RK4)	Species (semi-implicit midpoint)
1	$\boldsymbol{f}^{n} = \boldsymbol{f}\left(\boldsymbol{Q}^{n}, (\rho \boldsymbol{Y})^{n}\right)$	$\boldsymbol{k}_1 = \Delta t \boldsymbol{f}_{\mathrm{Q}}^n$	$(\rho \mathbf{Y})_1^* = (\rho \mathbf{Y})^n + \left(\mathbf{I} + (\Delta t/2) \left(\dot{\boldsymbol{\omega}}^-/\mathbf{Y}\right)^n\right)^{-1} (\Delta t/2) \mathbf{f}_Y^n$
2	$\boldsymbol{f}^{(1)} = \boldsymbol{f} \left(\boldsymbol{Q}^{n} + \boldsymbol{k}_{1}/2, (\rho \boldsymbol{Y})_{1}^{*} \right)$	$\boldsymbol{k}_2 = \Delta t \boldsymbol{f}_{\mathrm{Q}}^{(1)}$	$(\rho \mathbf{Y})_2^* = (\rho \mathbf{Y})_1^* + \left(\mathbf{I} + (\Delta t/2) \left(\dot{\boldsymbol{\omega}}^-/\mathbf{Y}\right)_1^*\right)^{-1} \left((\rho \mathbf{Y})^n - (\rho \mathbf{Y})_1^* + (\Delta t/2) \mathbf{f}_1^{(1)}\right)$
3	$\boldsymbol{f}^{(2)} = \boldsymbol{f} \left(\boldsymbol{Q}^{n} + \boldsymbol{k}_{2}/2, (\rho \boldsymbol{Y})_{2}^{*} \right)$	$\boldsymbol{k}_3 = \Delta t \boldsymbol{f}_{\mathrm{Q}}^{(2)}$	$(\rho \mathbf{Y})_{3}^{n+1} = 2(\rho \mathbf{Y})_{2}^{*} - (\rho \mathbf{Y})^{n} + \left(\mathbf{I} + (\Delta t/2) \left(\dot{\boldsymbol{\omega}}^{-}/\mathbf{Y}\right)_{2}^{*}\right)^{-1} \left(2\left[(\rho \mathbf{Y})^{n} - (\rho \mathbf{Y})_{2}^{*}\right] + \Delta t \boldsymbol{f}_{Y}^{(2)}\right)$
4	$\boldsymbol{f}^{(3)} = \boldsymbol{f}\left(\boldsymbol{Q}^{n} + \boldsymbol{k}_{3}, (\rho \boldsymbol{Y})_{3}^{n+1}\right)$	$\boldsymbol{k}_4 = \Delta t \boldsymbol{f}_{\mathrm{Q}}^{(3)}$	$(\rho \mathbf{Y})_{4}^{n+1} = (\rho \mathbf{Y})_{3}^{n+1} + \left(\mathbf{I} + (\Delta t/2) \left(\dot{\boldsymbol{\omega}}^{-}/\mathbf{Y}\right)_{3}^{n+1}\right)^{-1} \left((\rho \mathbf{Y})^{n} - (\rho \mathbf{Y})_{3}^{n+1} + (\Delta t/2) \left(\mathbf{f}_{Y}^{n} + (\Delta t/2)\right)^{-1} + (\Delta t/2) \left(\mathbf{f}_{Y}^{n} + (\Delta t/2)\right)^{-1} + (\Delta t/2) \left(\dot{\boldsymbol{\omega}}^{-}/\mathbf{Y}\right)_{3}^{n+1} + (\Delta t/2) \left(\dot{\boldsymbol{\omega}}^{-}$
			$f_{\gamma}^{(3)}))$

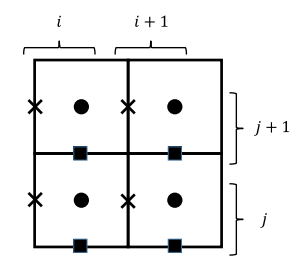


Fig. 1. Staggered grid arrangement in 2D. The scalars are stored at the cell centers (circles), the x-momentum on the vertical edges (crosses), and the y-momentum on the horizontal edges (squares).

completed with $\mathbf{Q}^{n+1} = \mathbf{Q}^n + \mathbf{k}_1/6 + \mathbf{k}_2/3 + \mathbf{k}_3/3 + \mathbf{k}_4/6$, and $(\rho \mathbf{Y})^{n+1} = (\rho \mathbf{Y})_4^{n+1}$. In the absence of semi-implicit correction, the first three iterations of the iterative explicit midpoint method and the first three stages of the RK4 scheme are mathematically identical, which is what makes the embedding simple.

As part of the evaluation of f, Y is obtained as $Y = (\rho Y)/\sum_{s=1}^{n_s} (\rho Y)_s$. This specification is important since discretely $\rho \neq \sum_{s=1}^{n_s} (\rho Y)_s$, as a result of using different time integrators for continuity and the species transport equations. The discrepancy between ρ and $\sum_{s=1}^{n_s} (\rho Y)_s$ is quantified in Sec. 3.2. Finally, in the absence of mixing and/or chemistry, this approach reverts to the RK4 scheme and is hence 4th order. This property is verified in Sec. 3.2.3.

2.3. Spatial discretization

The compressible solver used in this work is based on the code developed by Boeck et al. [9], which is itself based on the low Mach number flow solver NGA [10]. The compressible and low Mach number solvers share a lot in common, especially regarding the spatial discretization. We briefly review the discretization and only point out the differences between the low Mach and fully compressible discretizations. The reader is referred to Ref. [10] for more details.

To improve the accuracy of the divergence term in the continuity equation, the computational grid is staggered in space, i.e., the scalars are stored at the cell centers, while momentum is stored at the cell faces. This arrangement is depicted in Fig. 1 for a two-dimensional mesh. We perform simulations on a uniform Cartesian mesh. We use second-order accurate interpolation and differentiation stencils. In the x_1 direction, they are given by

$$\overline{\psi}^{x_1} = \frac{\psi(x_1 + \Delta x_1/2, x_2, x_3) + \psi(x_1 - \Delta x_1/2, x_2, x_3)}{2}, \quad \frac{\delta \psi}{\delta x_1} = \frac{\psi(x_1 + \Delta x_1/2, x_2, x_3) - \psi(x_1 - \Delta x_1/2, x_2, x_3)}{\Delta x_1}, \quad (12)$$

and are similarly defined in the x_2 and x_3 directions. Defining $g_i = \rho u_i$, the semi-discrete continuity equation is identical to its low Mach counterpart and is given by

$$\frac{\partial \rho}{\partial t} + \sum_{i=1}^{3} \frac{\delta g_i}{\delta x_i} = 0. \tag{13}$$

The treatment of the momentum equation and species transport equations is identical to the one given in [10]. The third-order Bounded QUICK scheme [13] is used for the species transport. For the energy equation, the convective term is discretized using central differences.

The compressible formulation requires the discretization of two additional terms compared to the low Mach number formulation. First, to determine the temperature (Eq. (5)), the term ρuu is computed as $\sum_{i=1}^{3} \overline{g_i u_i}^{x_i}$ to be consistent with the low Mach formulation (see Eq. 22 in Ref. [10]). Second, the spatial discretization of the viscous term in the energy equation is given by

$$\sum_{i=1}^{3} \left(\frac{\delta}{\delta x_{i}} \left(\sum_{j=1}^{3} \left(\overline{\overline{u_{j}^{x_{j}}}}^{x_{i}} \overline{\mu}^{x_{i}} \left(\overline{\widetilde{u_{i,j}}}^{x_{i}} + \overline{\widetilde{u_{j,i}}}^{x_{i}} - \frac{2}{3} \sum_{k=1}^{3} \overline{\widetilde{u_{k,k}}}^{x_{i}} \delta_{ij} \right) \right) \right) \right), \tag{14}$$

where δ_{ii} is the Kronecker delta, and

$$\widetilde{u_{i,j}} = \frac{\delta}{\delta x_i} \left(\overline{\overline{u_i}}_i^{x_i} x_j \right) \,. \tag{15}$$

Unnecessary interpolations are avoided, e.g., $\widetilde{u_{i,i}} = \delta u_i / \delta x_i$.

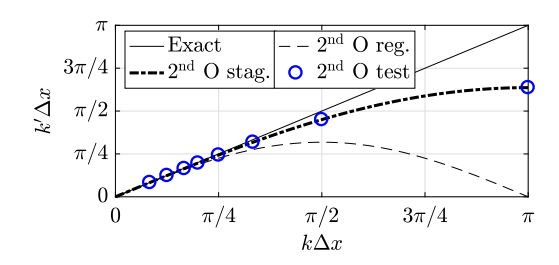


Fig. 2. Modified wavenumber diagram. The numerical results are shown by blue circles. The thick and thin dashed lines show the analytical wavenumber relations for staggered and non-staggered grids, respectively. The solid line is the theoretical relation in absence of dispersion errors. (For interpretation of the colors in the figure(s), the reader is referred to the web version of this article.)

3. Results

We first verify that the solver behaves as expected for non-reacting flows. We then proceed with reacting flows, focusing on the performance of the proposed time integration scheme.

3.1. Verification: non-reacting cases

To assess the spatial accuracy, we perform a series of inviscid one-dimensional simulations, including a traveling acoustic wave and an entropy wave in periodic domains. The first flow configuration is specific to the compressible formulation, whereas the second one assesses the ability of the solver to capture large density gradients typical of reacting flows.

3.1.1. Traveling acoustic wave

A one-dimensional traveling acoustic wave is the solution to the linearized Navier-Stokes equations with the following initial conditions

$$p = p_0 + f(kx), \qquad \rho = \rho_0 + \frac{1}{c_0^2} f(kx), \qquad u = \frac{1}{\rho_0 c_0} f(kx), \qquad \rho e_t = \frac{p}{\gamma - 1} + \frac{\rho u^2}{2}, \tag{16}$$

where c_0 is the sound speed, k is the wavenumber, and $\omega = kc_0$ is the angular frequency. The computational domain is periodic with length L. We choose a sinusoidal initial pressure field $f(kx) = A_p \sin(kx)$, and $k = 2\pi/L$. Since the solution given by Eq. (16) is valid for $A_p \ll p_0$ only, we choose $A_p = 10^{-5} p_0$.

As discussed in Sec. 2.3, we use second-order central differentiation operators. These schemes are not diffusive, however they introduce dispersion errors. When solving a simple advection equation, i.e.,

$$\frac{\partial \phi}{\partial t} + a \frac{\partial \phi}{\partial y} = 0, \tag{17}$$

this causes waves $\phi_k(x) = \sin(kx)$ to move at a modified speed a' that depends on the wavenumber k. This behavior is traditionally characterized with a modified wavenumber diagram such as the one presented in Fig. 2. For the simple advection equation, the modified wavenumber k' is related to a' by

$$k' = \frac{ka'}{a}. (18)$$

In the context of acoustics, dispersion errors cause waves to move at a modified sound speed c_0' . In Fig. 2, the blue circles show the numerical modified wavenumber relations observed numerically. We evaluate k' by using Eq. (18) with $a' = c_0'$. The latter is computed as $c_0' = L/t_{travel}$, where t_{travel} is the time it takes for the acoustic wave to travel the length of the domain, evaluated by fitting a sine wave to p(x = 0, t). The thick dashed line shows the analytical modified wavenumber relation for a staggered grid arrangement. The thin dashed line shows the relation for a regular (i.e., non-staggered) grid to emphasize the improved accuracy obtained by using a staggered grid. The analytical and numerical results are in excellent agreement.

3.1.2. Entropy wave

To further assess the spatial accuracy, we perform a series of inviscid simulations of entropy waves being convected at a uniform velocity u_{∞} in a 1D periodic domain. The initial fields are

$$u = u_{\infty}, \qquad p = p_0, \qquad \rho = \rho_0 + g(x), \qquad (\rho e_t) = \frac{p_0}{\gamma - 1} + \frac{\rho u_{\infty}^2}{2}.$$
 (19)

We choose $u_{\infty} = c_0/2$ and the following density distribution

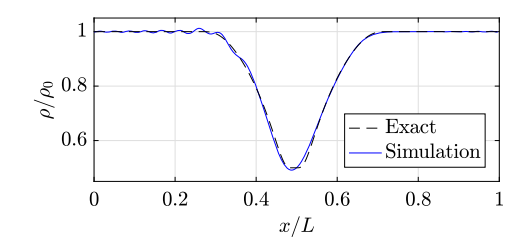


Fig. 3. Comparison of the initial density field (dashed line) with the numerical solution at $t_f = L/u_\infty$ for $L/\Delta x = 256$ (solid line).

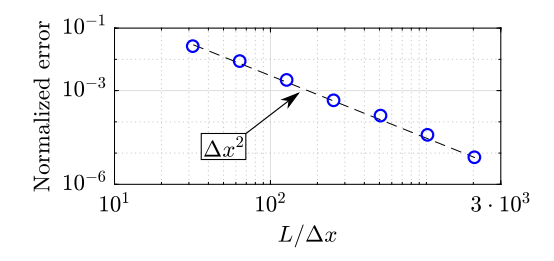


Fig. 4. Normalized error of the numerical solution of Eq. (19) at $t_f = L/u_{\infty}$ for different spatial resolutions.

$$g(x) = \begin{cases} -\alpha \rho_0 (1 - \exp(-R\kappa/x \exp(R/(x - R)))) & \text{if } |x| \le R \\ 0 & \text{if } |x| > R \end{cases},$$
 (20)

which is C^{∞} and has compact support. We set $\alpha=0.5$, $\kappa=1$, and R=L/4. We run the simulation for one flow-through time, i.e., $t_f=L/u_{\infty}$. The initial and final density field are shown in Fig. 3 for a simulation with $L/\Delta x=256$. Small oscillations in the wake of the density profile can be observed and are characteristics of centered schemes.

The normalized error, computed as

$$\sqrt{\int_{x}^{\infty} \left(\rho(x,t_f) - \rho(x,0)\right)^2 dx} / \int_{x}^{\infty} \rho(x,0)^2 dx$$

is shown in Fig. 4 for different spatial resolutions. The expected order of convergence (namely second) is observed.

3.2. Main results: reacting cases

The focus of this paper is on flows in which both transport and chemistry are present. Hence, we do not consider homogeneous reactors. Instead, we look at premixed flames as they are a perfect example of the tight coupling between chemistry and transport. We consider the combustion of a premixed n-heptane/air mixture under standard conditions and $\phi=0.9$. The two flow configurations studied are a one-dimensional flat flame, and a statistically-stationary three-dimensional turbulent case.

3.2.1. Chemical models

We provide results using the same detailed chemical model used by Savard et al. [14], referred to as Mechanism #1. It includes 35 species and 217 reactions. For the one-dimensional case, we also carry out simulations using JetSurF version 2.0 [15], from which the aromatic species and the molecules containing more than 7 carbon atoms have been removed, which is justified by the slightly lean conditions considered. This reduced model is referred to as Mechanism #2, and contains 180 species and 2168 reactions.

The inverses of the eigenvalues of the chemical Jacobian $\tau_{\text{Jac},\,\text{full}}$ correspond to the different chemical timescales of the system [2]. They are plotted in Fig. 5 for the two mechanisms considered. The chemical Jacobians are evaluated in the flame at the location of maximum heat release, using the one-dimensional flat flame configuration. The species associated with each eigenvalue can be determined using the approximation of the diagonal of the chemical Jacobian detailed in Sec. 2.2. As shown in Fig. 5a, the two smallest timescales for Mechanism #1 are $\mathcal{O}(10^{-9}\text{s})$ and are associated with the pentyl and heptyl radicals. For Mechanism #2, the smallest timescale is $\mathcal{O}(10^{-14}\text{s})$ and is also associated with a pentyl radical. However, it is smaller than for Mechanism #1 by six orders of magnitude. After careful inspection of the thermodynamic properties of $2-C_5H_{11}$, we found out that its enthalpy of formation was erroneous. More precisely, it is about 115kJ/mol higher than for 1-pentyl radicals, whereas the values for 2-alkyl radicals are commonly lower than for 1-alkyl radicals by about 10kJ/mol [16].

A new chemical Jacobian was computed, using the thermodynamic properties of $3 - C_5H_{11}$ instead of the original ones for $2 - C_5H_{11}$. For this new chemical Jacobian, the timescale associated with $2 - C_5H_{11}$ is significantly larger, and closer

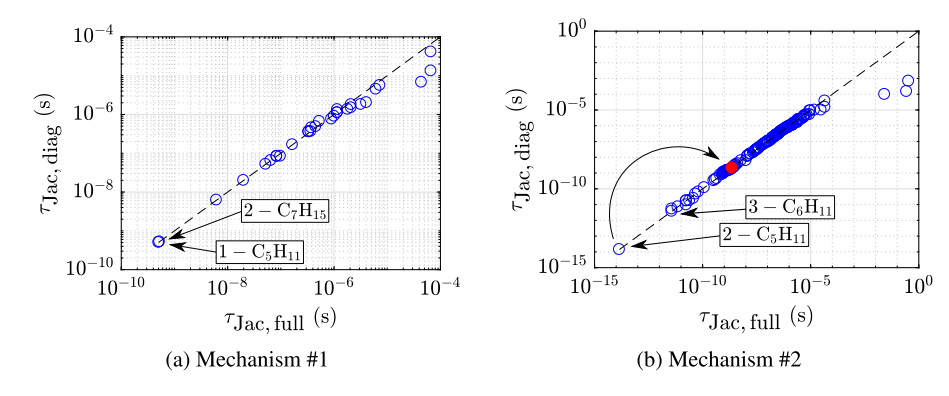


Fig. 5. Comparison of the timescales for the full chemical Jacobian $\tau_{\text{Jac, full}}$ and its diagonal approximation $\tau_{\text{Jac, diag.}}$

to the other pentyl radicals. It is shown by the red dot in Fig. 5b. It is possible that JetSurF version 2.0 suffers from other issues that artificially increase its stiffness. However, the goal of this paper is to show that the proposed integration scheme can handle very stiff mechanisms well. That is why, the unmodified JetSurF mechanism will be used for all simulations.

3.2.2. Freely propagating one-dimensional flame

We now consider a one-dimensional flat n-heptane/air premixed flame at $\phi=0.9$. The flame is freely propagating in a still unburnt mixture. We first show results obtained using Mechanism #1. Fig. 6a shows the mass fraction of 1-pentyl radical as a function of temperature, using the proposed method with $\Delta t=2\cdot 10^{-8}$ s (corresponding to an acoustic CFL of 0.9), and using the RK4 scheme for the species with $\Delta t=5\cdot 10^{-10}$ s and $\Delta t=2\cdot 10^{-8}$ s. The 1-pentyl radical is chosen since it is associated with the largest eigenvalue (smallest timescale) of the chemical Jacobian. Clearly, the simulation using the RK4 scheme for the species with $\Delta t=2\cdot 10^{-8}$ s is unstable, and predicts negative pentyl mass fractions. In contrast, the results obtained using the proposed method with $\Delta t=2\cdot 10^{-8}$ s are in excellent agreement with the results obtained using the RK4 scheme for the species with $\Delta t=5\cdot 10^{-10}$ s. The accuracy plot shown in Fig. 6b confirms that the overall approach yields 2nd order accurate results in time, as expected. The normalized errors for the different species are evaluated in temperature space as

$$\sqrt{\int\limits_T \left(Y_s - Y_{s,ref}\right)^2 dT} / \int\limits_T Y_{s,ref}^2 dT ,$$

with a reference solution $Y_{s,ref}$ obtained with $\Delta t = 10^{-10}$ s.

The results obtained with Mechanism #2 are shown in Fig. 7. Fig. 7a shows the mass fraction of $2-C_5H_{11}$ in temperature space, using the proposed framework with $\Delta t = 2\cdot 10^{-8}$ s, and using the RK4 scheme with $\Delta t = 10^{-12}$ s and $\Delta t = 10^{-15}$ s. First, one observes that max($Y_{2-C_5H_{11}}$) is very small, as a result of the erroneously short consumption timescale generated by the chemical Jacobian (Fig. 5b). Second, using the RK4 scheme for the species with $\Delta t = 10^{-12}$ s yields unphysical results, as the chemical timescale associated with $2-C_5H_{11}$ is much smaller ($\tau_{2-C_5H_{11}}\sim 10^{-14}$ s). Third, the results obtained using the proposed approach with $\Delta t = 2\cdot 10^{-8}$ s are in excellent agreement with the ones obtained employing the RK4 scheme for the species with $\Delta t = 10^{-15}$ s. Fig. 7b shows the temporal accuracy for different species, which is found to be 2nd order accurate. For very small timesteps, the error for $2-C_5H_{11}$ plateaus, which is likely due to its tiny mass fraction compared to the other species.

As discussed in Sec. 2.2.3, using two different time integrators introduces inconsistencies between the density field obtained from continuity and the one given by the species mass fractions, i.e., $\rho \neq \sum_{s=1}^{n_s} (\rho Y)_s$. To quantify this error, we compute the normalized density error $\epsilon = |\rho - \sum_s (\rho Y)_s|/\rho$ for the two cases considered in this section. This quantity is found to be small, i.e., $\max(\epsilon) = 4 \cdot 10^{-6}$ when using Mechanism #1 and $\max(\epsilon) = 5 \cdot 10^{-5}$ when using Mechanism #2. In summary, the method described in this work stabilizes the solution and yields 2nd order accurate results for the species mass fractions, while introducing minimal discrepancies between the two density fields.

3.2.3. Interaction of an acoustic wave with a one-dimensional flame

In this section, flame-acoustics interactions are investigated by looking at the dynamics of an acoustic wave impacting the one-dimensional flame considered in Sec. 3.2.2. The goal is to determine the accuracy of the proposed time integration scheme for the transport of acoustic waves. We employ Mechanism #1. A right-traveling acoustic wave is initially introduced ahead of the flame. Its pressure profile is shown by a solid black line labeled A in Fig. 8a. First, the wave travels from $A \rightarrow B$ in the unburnt mixture. Then, from $B \rightarrow C$, the wave is partially transmitted/reflected by the flame. To evaluate the temporal accuracy, we extract (ρu) at the locations where $|p - p_0|$ is maximum, shown by the red stars in Fig. 8a. In Fig. 8b, we show the accuracy of the proposed method for each of the two segments $(\psi = (\rho u))$. The scheme is seen to be 4th order

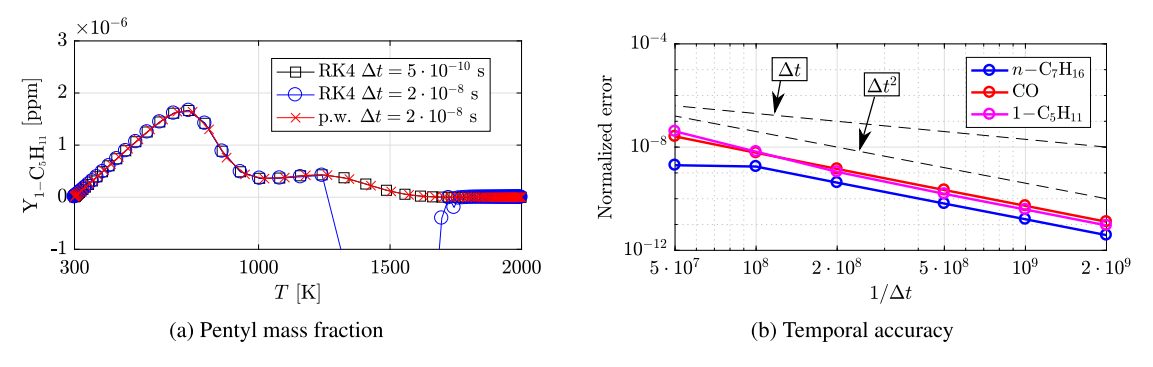


Fig. 6. Performance of the proposed method for the laminar one-dimensional case using Mechanism #1.

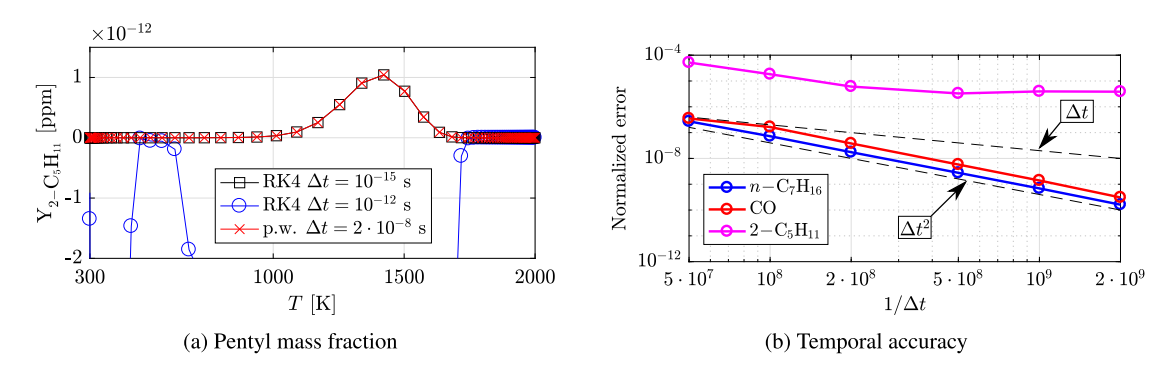


Fig. 7. Performance of the proposed method for the laminar one-dimensional case using Mechanism #2.

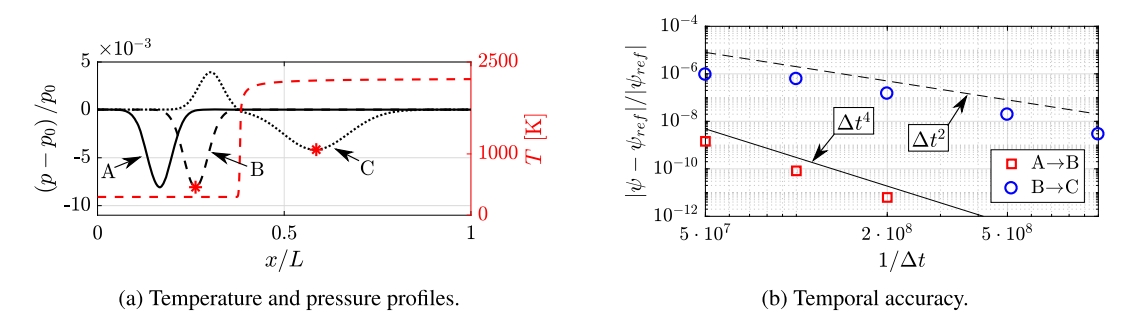


Fig. 8. Results for an acoustic wave impinging on a one-dimensional flame.

accurate for $A \to B$, where there is no chemistry nor mixing. From $B \to C$, as the acoustic wave goes through the flame, the scheme is 2nd order accurate, as expected.

3.2.4. Turbulent flame

We now examine a turbulent case, which corresponds to Flame C_1 in Lapointe et al. [11]. The unburnt temperature is $T_u=800$ K, pressure is p=1 atm, and Mechanism #1 is used. Two-dimensional slices showing temperature and pentyl mass fraction isocontours are shown in Fig. 9. These results are obtained with $\Delta t=10^{-8}$ s, which corresponds to an acoustic CFL of 0.9. This configuration remains entirely subsonic, with local Mach numbers reaching 0.5. Fig. 10 shows the joint probability density function of pentyl mass fraction and temperature for simulations performed using the original RK4 scheme for the species, and the proposed method. Again, negative mass fractions are predicted when using the RK4 scheme for the species transport with $\Delta t=10^{-8}$ s, a problem which is solved using the framework presented in this work.

Fig. 11 shows the spatial distribution of the normalized density error ϵ . This error is concentrated in the turbulent flame brush and disappears on the burnt side. In Fig. 12, we quantify this error as a function of time for three different timestep sizes. All simulations are such that $\rho = \sum_s (\rho Y)_s$ initially. Time is normalized with the eddy turnover time τ_0 . In all cases, the errors remains bounded and almost constant over time at a value determined by the timestep size. Three phenomena contribute to ϵ : the different time integrators for continuity (RK4) and for the species transport (midpoint), the semi-implicit treatment of chemistry, and the use of a non-linear spatial transport scheme for the species mass fractions. The combined error due to the semi-implicit treatment of chemistry and the different time integrators is expected to decrease with the

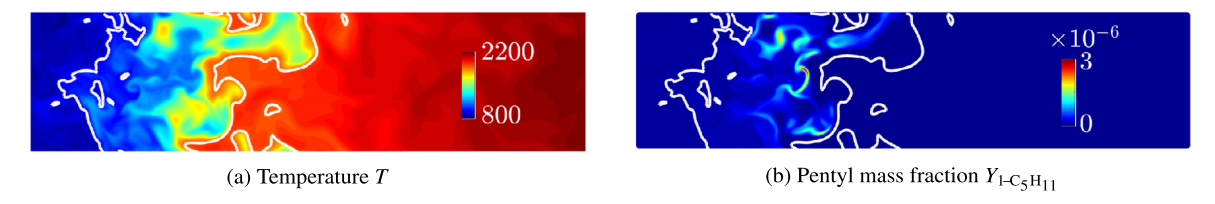


Fig. 9. Two-dimensional slices showing isocontours for the turbulent case ($\Delta t = 10^{-8}$ s). Two temperature isolines are superimposed in white (T = 1000 K and T = 1900 K).

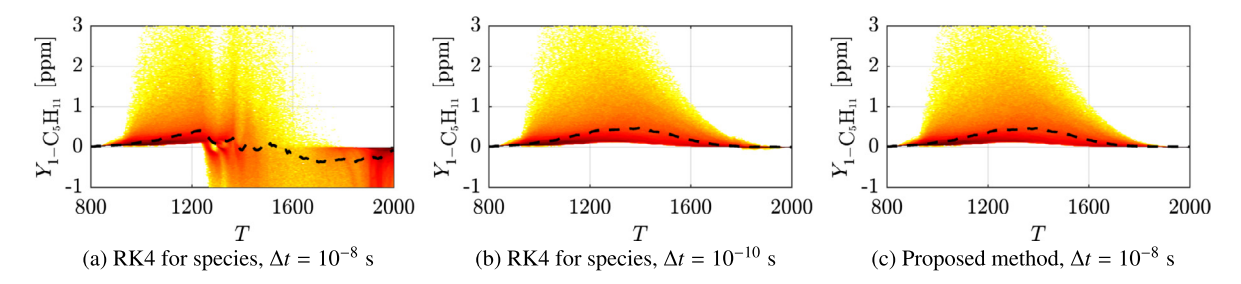


Fig. 10. Joint probability density function of pentyl mass fraction and temperature for the turbulent case. The black dashed line represents the conditional mean.

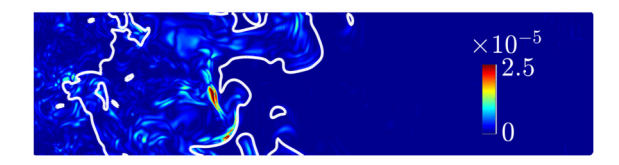


Fig. 11. Two-dimensional slice showing isocontours of ϵ for the turbulent case ($\Delta t = 10^{-8}$ s). Two temperature isolines are superimposed in white (T = 1000 K and T = 1900 K).

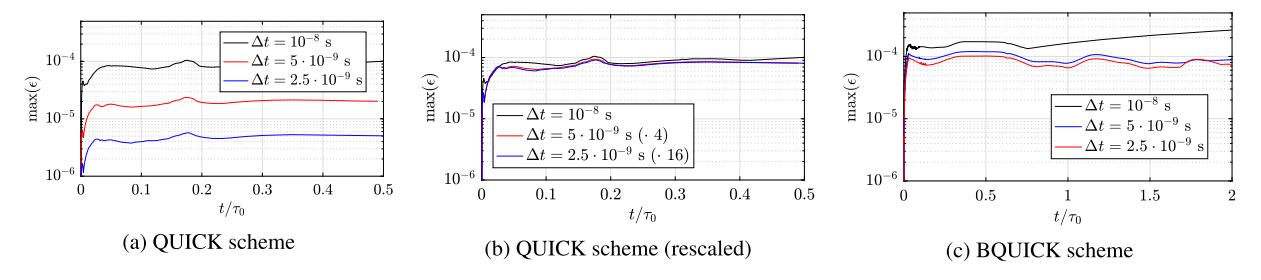


Fig. 12. Maximum density error $\max(\epsilon)$ as a function of time for the turbulent case, using different schemes for the species transport.

timestep size as Δt^2 , since the proposed method blends a 2nd midpoint method and the 4th order RK4 scheme. To explore this further, we present in Figs. 12a and 12b results obtained with the linear transport scheme QUICK [17]. In this particular case, max $(\epsilon) \sim \Delta t^2$. This is highlighted in Fig. 12b, where max (ϵ) is rescaled by assuming a 2nd order convergence rate.

The error due to the scalar transport scheme deserves more attention. The BQUICK scheme, along with other popular transport schemes such as WENO [18] and BCH [19], is non-linear. Non-linear schemes are desirable because they combine high accuracy, low dissipation, and boundedness. However, their non-linearity induces a discrepancy between the convective terms from the continuity equation (Eq. (1)) and the sum of the convective terms from the species transport equations (Eq. (4)), i.e., $\sum_s \nabla \cdot (\rho \mathbf{u} \mathbf{Y}_s)) \neq \nabla \cdot (\rho \mathbf{u})$. Hence, as shown in Fig. 12c, max (ϵ) decreases with the timestep size, but eventually reaches a plateau around max $(\epsilon) \sim 10^{-4}$. It should be noted that this error is not due to the proposed method and will be present anytime a non-linear scheme is used for the species transport equations. In all cases, the discrepancy between the two density fields remains very small.

4. Conclusion

The stiffness associated with the chemical source terms can severely impact the quality of a solution to the reacting Navier-Stokes equations when explicit time integration schemes are used. In this paper, we presented a simple method to remove this stiffness when the RK4 scheme is employed. We solve the species transport equations with the semi-implicit midpoint method proposed by Savard et al. [2], and we employ the RK4 scheme for the integration of the other flow

variables. Using laminar and turbulent premixed *n*-heptane / air flames as examples, we showed that the proposed method stabilizes the simulations, and yields accurate results. Specifically, the method was shown to be second-order accurate in the presence of chemistry and/or mixing, and fourth-order accurate otherwise.

Declaration of competing interest

The authors declare that they have no known competing financial interests or personal relationships that could have appeared to influence the work reported in this paper.

Acknowledgements

The authors gratefully acknowledge funding from the Natural Sciences and Engineering Council of Canada (NSERC Post-graduate Scholarship D) and the Foster and Coco Stanback Space Innovation Fund. This work used the Extreme Science and Engineering Discovery Environment (XSEDE), which is supported by National Science Foundation grant number ACI-1053575.

References

- [1] T. Lu. C.K. Law. C.S. Yoo, I.H. Chen, Dynamic stiffness removal for direct numerical simulations, Combust, Flame 156 (2009) 1542–1551.
- [2] B. Savard, Y. Xuan, B. Bobbitt, G. Blanquart, A computationally-efficient, semi-implicit, iterative method for the time-integration of reacting flows with stiff chemistry, J. Comput. Phys. 295 (2015) 740–769.
- [3] S.H. Lam, D.A. Goussis, Understanding complex chemical kinetics with computational singular perturbation, Symp., Int., Combust. 22 (1989) 931–941.
- [4] U. Maas, S.B. Pope, Simplifying chemical kinetics: intrinsic low-dimensional manifolds in composition space, Combust. Flame 88 (1992) 239-264.
- [5] S.D. Cohen, A.C. Hindmarsh, P.F. Dubois, CVODE, a stiff/nonstiff ODE solver in C, Comput. Phys. 10 (1996) 138-143.
- [6] B. Sportisse, An analysis of operator splitting techniques in the stiff case, J. Comput. Phys. 161 (2000) 140-168.
- [7] J.H. Chen, A. Choudhary, B. De Supinski, M. DeVries, E.R. Hawkes, S. Klasky, W.-K. Liao, K.-L. Ma, J. Mellor-Crummey, N. Podhorszki, et al., Terascale direct numerical simulations of turbulent combustion using S3D, Comput. Sci. Discov. 2 (2009) 15001.
- [8] T. Colonius, S.K. Lele, Computational aeroacoustics: progress on nonlinear problems of sound generation, Prog. Aerosp. Sci. 40 (2004) 345-416.
- [9] L. Boeck, S. Lapointe, J. Melguizo-Gavilanes, G. Ciccarelli, Flame propagation across an obstacle: OH-PLIF and 2-D simulations with detailed chemistry, Proc. Combust. Inst. 000 (2016) 1–8.
- [10] O. Desjardins, G. Blanquart, G. Balarac, H. Pitsch, High order conservative finite difference scheme for variable density low Mach number turbulent flows, J. Comput. Phys. 227 (2008) 7125–7159.
- [11] S. Lapointe, B. Savard, G. Blanquart, Differential diffusion effects, distributed burning, and local extinctions in high Karlovitz premixed flames, Combust. Flame 162 (2015) 3341–3355.
- [12] J.F. MacArt, M.E. Mueller, Semi-implicit iterative methods for low Mach number turbulent reacting flows: operator splitting versus approximate factorization, J. Comput. Phys. 326 (2016) 569–595.
- [13] M. Herrmann, G. Blanquart, V. Raman, Flux corrected finite volume scheme for preserving scalar boundedness in reacting large-eddy simulations, AIAA J. 44 (2006) 2879–2886.
- [14] B. Savard, B. Bobbitt, G. Blanquart, Structure of a high Karlovitz n-C7H16 premixed turbulent flame, Proc. Combust. Inst. 35 (2015) 1377-1384.
- [15] R.P.L.H. Wang, E. Dames, B. Sirjean, D.A. Sheen, R. Tango, A. Violi, J.Y.W. Lai, F.N. Egolfopoulos, D.F. Davidson, R.K. Hanson, C.T. Bowman, C.K. Law, W. Tsang, N.P. Cernansky, D.L. Miller, A high-temperature chemical kinetic model of n-alkane (up to n-dodecane), cyclohexane, and methyl-, ethyl-, n-propyl and n-butyl-cyclohexane oxidation at high temperatures, JetSurF v. 2.0, 2010, http://web.stanford.edu/group/haiwanglab/, 2010, http://web.stanford.edu/group/haiwangla
- [16] C.F. Goldsmith, G.R. Magoon, W.H. Green, Database of small molecule thermochemistry for combustion, J. Phys. Chem. A 116 (2012) 9033–9057.
- [17] B.P. Leonard, A stable and accurate convective modelling procedure based on quadratic upstream interpolation, Comput. Methods Appl. Mech. Eng. 19 (1979) 59–98
- [18] G.-S. Jiang, D. Peng, Weighted ENO schemes for Hamilton-Jacobi equations, SIAM J. Sci. Comput. 21 (2000) 2126-2143.
- [19] S. Verma, Y. Xuan, G. Blanquart, An improved bounded semi-Lagrangian scheme for the turbulent transport of passive scalars, J. Comput. Phys. 272 (2014) 1–22.